

## Article

# Structural Analysis and 3D Reconstruction of Underground Pipeline Systems Based on LiDAR Point Clouds

Qiuyao Lai, Qinchuan Xin , Yuhang Tian, Xiaoyou Chen, Yujie Li and Ruohan Wu \*

School of Geography and Planning, Sun Yat-sen University, Guangzhou 510275, China; laiqy9@mail2.sysu.edu.cn (Q.L.); xinqinchuan@mail.sysu.edu.cn (Q.X.); tianyh25@mail2.sysu.edu.cn (Y.T.); chenxy956@mail2.sysu.edu.cn (X.C.); liyj365@mail2.sysu.edu.cn (Y.L.)

\* Correspondence: wurh35@mail.sysu.edu.cn

**Abstract:** The underground pipeline is a critical component of urban water supply and drainage infrastructure. However, the absence of accurate pipe information frequently leads to construction delays and cost overruns, adversely impacting urban management and economic development. To address these challenges, the digital management of underground pipelines has become essential. Despite its importance, research on the structural analysis and reconstruction of underground pipelines remains limited, primarily due to the complexity of underground environments and the technical constraints of LiDAR technology. This study proposes a framework for reconstructing underground pipelines based on unstructured point cloud data, aiming to accurately identify and reconstruct pipe structures from complex scenes. The Random Sample Consensus (RANSAC) algorithm, enhanced with parameter-adaptive adjustments and subset-independent fitting strategies, is employed to fit centerline segments from the set of center points. These segments were used to reconstruct topological connections, and a Building Information Model (BIM) of the underground pipeline was generated based on the structural analysis. Experiments on actual underground scenes evaluated the method using recall rate, radius error, and deviation between point clouds and models. Results showed an 88.8% recall rate, an average relative radius error below 3%, and a deviation of 3.79 cm, demonstrating the framework's accuracy. This research provides crucial support for pipeline management and planning in smart city development.



Academic Editor: Sara  
Gonizzi Barsanti

Received: 5 December 2024

Revised: 7 January 2025

Accepted: 15 January 2025

Published: 20 January 2025

**Citation:** Lai, Q.; Xin, Q.; Tian, Y.; Chen, X.; Li, Y.; Wu, R. Structural Analysis and 3D Reconstruction of Underground Pipeline Systems Based on LiDAR Point Clouds. *Remote Sens.* **2025**, *17*, 341. <https://doi.org/10.3390/rs17020341>

**Copyright:** © 2025 by the authors. Licensee MDPI, Basel, Switzerland. This article is an open access article distributed under the terms and conditions of the Creative Commons Attribution (CC BY) license (<https://creativecommons.org/licenses/by/4.0/>).

**Keywords:** underground pipeline; 3D reconstruction; point clouds; building information model; RANSAC algorithm

## 1. Introduction

The underground pipeline system includes pipes used for water supply, drainage, natural gas, and electricity, forming a critical component of urban underground infrastructure [1–3]. However, discrepancies between the designed and actual pipeline, arising from construction errors, design changes, and the complexity of the underground environment, are common. Such deviations exacerbate maintenance and management challenges, leading to construction delays, cost overruns, and conflicts with existing utilities. These issues can result in utility outages, project disruptions, and elevated risks to urban operations. Consequently, accurate and efficient digital information of underground pipelines is crucial for urban management and the maintenance of essential services.

Building Information Modeling (BIM) has emerged as a powerful tool for managing both above-ground and underground infrastructure. It supports the creation, management, and maintenance of digital representations of structures throughout their lifecycle [4].

Within urban infrastructure, BIM integrates and coordinates various information, facilitating the visualization and management of underground pipes [5]. Recently, the advancements in remote sensing technologies have provided new opportunities for modeling of pipeline systems [6]. Among these technologies, LiDAR has proven particularly valuable due to its ability to capture high-resolution three-dimensional data of terrain and objects through laser-based distance measurements, and is widely applied in the Architecture, Engineering, and Construction (AEC) industry [7–11]. LiDAR offers several advantages over traditional surveying methods, including non-invasive point cloud collection and minimal disruption to existing infrastructure [12]. The resulting point cloud data serve as a reliable data foundation for the creation of BIMs of pipeline systems [13,14]. Significant efforts have been directed toward developing efficient frameworks for pipeline system reconstruction using high-resolution point cloud data [15–18]. The key to modeling underground pipeline systems lies in the accurate detection of pipeline structures, which predominantly exhibit cylindrical geometry. A bottom-up approach simplifies the problem by reducing pipe detection to a cylinder detection challenge, enabling more intuitive and efficient modeling. Commonly used methods of cylinder detection include Random Sample Consensus (RANSAC) [19], region growing [20], and Hough transform algorithms. The RANSAC algorithm fits models by iteratively sampling random subsets of points and evaluates the model quality based on fitting errors [21]. Liu et al. [22] applied the RANSAC algorithm to detect circular features by projecting pipe structures onto a plane. However, this approach is limited to pipelines that are either vertical or parallel to the ground. Jin and Lee [23] introduced a RANSAC-based sphere fitting method, which involved rolling spheres of uniform diameter along the cylinder interior to determine its central axis. While innovative, this method is highly susceptible to noise and inaccuracies, particularly in scenarios with sparse or incomplete point cloud data. The region growing algorithm segments point cloud data by analyzing the similarity between seed points and their neighboring points. Kawashima, Kanai, and Date [16] applied a normal-based region growing method to extract pipe points, transforming 3D cylinder detection into a 2D projection plane circle fitting problem. Li et al. [24] combined density-based clustering and region growing algorithms to accurately extract geometric features, but this method is only suitable for straight pipes. The region growing method is sensitive to similarity measures and parameter selection, and improper choices can introduce errors, especially when dealing with noisy data. The Hough transform maps data points to parameter space and detects specific geometric shapes through a voting mechanism. Ahmed et al. [25] sliced the point cloud and projected it at equal intervals, using a 2D Hough transform for circle detection in each slice. The main challenge with the classical Hough transform is its memory requirements and computation time. To address this, Figueiredo et al. [26] and Patil et al. [27], inspired by the work of Rabbani and Van Den Heuvel [28], proposed staged Hough transform approaches to reduce complexity, respectively.

Despite these advancements, bottom-up methods often lack a global perspective, posing significant challenges in the reconstruction of topological connections of pipelines. To address these challenges, some studies have employed skeletonization techniques to derive the pipeline's central axis with geometric and topological features [29–31]. For instance, Lee et al. [32] extracted the skeleton based on Voronoi diagrams and topological refinement methods, enabling component segmentation by analyzing node connectivity and acute angles between adjacent nodes. Additionally, curvature-based methods [33] and RANSAC-based methods [34] have been applied to estimate skeleton nodes effectively. More recently, deep learning models, such as convolutional neural networks [35], and the innovative PipeNet framework [17], have demonstrated promising applications in pipeline reconstruction.

Current research predominantly focuses on relatively controlled and accessible building environments, such as mechanical, electrical, and plumbing (MEP) systems and industrial plants, where precise and multi-angle on-site measurements ensure high-quality data collection [17,27,33,36]. However, pipeline reconstruction in underground environments poses numerous challenges. The complex underground conditions and cluttered surface cover often lead to occlusions and indistinct surface features. These issues result in sparse and incomplete point cloud data, complicating the development of models that meet precision requirements for practical applications.

To address these limitations, this study proposes a framework for underground pipeline reconstruction based on unstructured point clouds. The proposed framework, which requires no prior assumptions, is capable of processing pipes with arbitrary orientation and size and constructing topologically connected underground pipeline models. First, the pipeline point cloud is derived through semantic segmentation. Subsequently, the geometric features of the pipes are utilized to preliminarily extract the central point set and radius information, with the central point set serving as input for subsequent structural analysis. To address data gaps and noise in the point cloud, this study proposes a centerline generation method combining a parameter-adaptive adjustment strategy and angle-distance metrics. This approach ultimately enables the analysis of pipe topological connections, facilitating the creation of high-precision underground pipe BIMs. The contributions of this framework include: (1) an improved RANSAC algorithm that effectively mitigates noise interference and enhances segmentation efficiency compared to traditional methods; (2) a parameter-adaptive adjustment strategy that enables the framework's applicability to pipes of various types and sizes; (3) a set of evaluation metrics based on angle and distance indicators which can reconnect fragmented straight pipe structures during refinement and reconstruct pipeline topological connections; (4) the achievement of high-precision underground pipeline reconstruction from incomplete point clouds to structured BIMs. This research significantly improves the efficiency of underground pipe management, facilitating the intelligent development of urban infrastructure. It also enhances the sustainability and adaptability of urban management practices, providing a robust foundation for the realization of the smart city.

## 2. Materials

The point cloud data used in this study are obtained from the underground pipeline system in the Sha Tin District of Hong Kong, using ground-based laser scanning equipment. The pipe network includes both freshwater and saltwater pipes. The dataset consists of 171 scan files stored in ASCII format, with each file containing the following attributes:  $\{x, y, z, r, g, b, \text{label}\}$ , where  $\{x, y, z\}$  represents the spatial coordinates,  $\{r, g, b\}$  denotes the color attribute, and  $\{\text{label}\}$  corresponds to the semantic label. The semantic labels are manually annotated and classified into two classes: pipe and non-pipe. This dataset is used to train and test the semantic segmentation network, which segments pipe data from complex underground environments, used for subsequent structural analysis and BIM reconstruction. Due to factors such as sensor resolution, viewpoint, light reflection, and pipe material, some pipe areas exhibit inconsistent or missing color information. Therefore, the RGB color attribute is excluded as an input feature for the semantic segmentation network. Instead, they are used as a reference during the BIM construction.

To validate the proposed reconstruction framework, three representative real-world scenes are selected based on segmented data. These scenes encompass different pipe arrangements, background complexities, and data quality levels. Scene A, derived from a freshwater pipeline system, presents a complex pipe layout and a cluttered background, with significant data missing due to occlusions. Its spatial dimensions

are  $104.05 \times 57.92 \times 6.45$  m. Scene B, also from a freshwater pipeline system, features a simpler pipe arrangement with some residual noise. Its spatial dimensions are  $43.11 \times 35.31 \times 5.84$  m. Scene C, from a saltwater pipeline system, represents a simple scene and high-quality data. Its spatial dimensions are  $106.60 \times 18.58 \times 11.19$  m. The basic statistical details of these scenes are shown in Table 1.

**Table 1.** Information of data for validation.

Scene	Pipe Type	Spatial Dimensions	No. of Scanned Files	No. of Points
Scene A	freshwater pipe	$104.05 \times 57.92 \times 6.45$ m	21	$4.11 \times 10^7$
Scene B	freshwater pipe	$106.60 \times 18.58 \times 11.19$ m	12	$2.90 \times 10^7$
Scene C	saltwater pipe	$43.11 \times 35.31 \times 5.84$ m	7	$2.03 \times 10^7$

### 3. Methods

Due to the harsh underground environment, object occlusions, and limitations of LiDAR technology, underground pipe data often suffer from missing data, along with noise and outliers, which complicates the pipe structure analysis. To address the issues, this study proposes a point cloud-based underground pipeline reconstruction framework designed to extract high-precision pipe topological information from incomplete point clouds.

The proposed framework consists of four main steps (as shown in Figure 1). First, the raw point cloud is preprocessed to isolate the underground pipe data and eliminate irrelevant points. Second, an initial set of central points and radius information of pipes is extracted. To mitigate the effects of sparse and missing data in the point cloud, normals are used for compensation. Third, a centerline generation method is proposed, incorporating parameter-adaptive adjustment strategies and introducing angle and distance metrics. The adaptive adjustment strategy optimizes the fitting range of the RANSAC algorithm, enabling its applicability to different types of pipes. The angle and distance metrics enhance the accuracy of the centerline. Finally, a topological connectivity analysis is conducted on centerline segments, ultimately generating the underground pipeline BIMs.

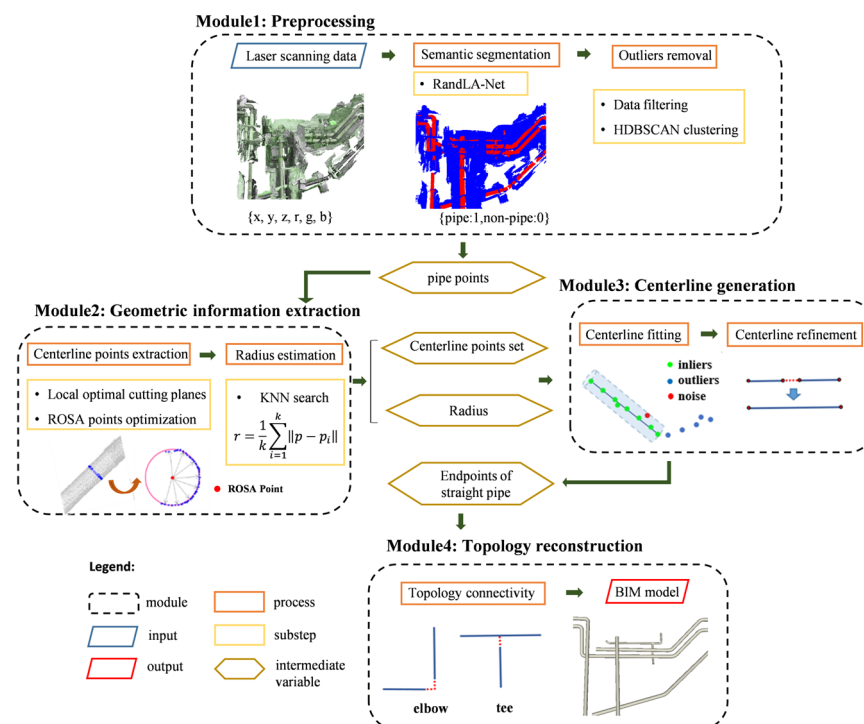


**Figure 1.** The flowchart of the proposed framework.

### 3.1. Data Preprocessing

Due to the complex background of point cloud data in real-world underground pipe scenes (including ground, markers, and fixed objects), this study first applies the RandLA-Net network for semantic segmentation of pipes. The segmentation results are then further optimized using clustering and filtering algorithms to improve the accuracy and reliability of pipe points extraction.

#### 3.1.1. Semantic Segmentation Based on RandLA-Net

Recent advancements in deep learning have revolutionized point cloud processing, with existing semantic segmentation networks having great potential in eliminating the influence of complex backgrounds. RandLA-Net, as an advanced semantic segmentation network, is capable of directly processing point clouds [37]. RandLA-Net utilizes multilayer perceptrons (MLPs) as its foundational components and integrates random sampling (RS) and local feature aggregation (LFA) modules, enabling efficient and accurate segmentation of underground pipe points. As shown in Figure 2a, RandLA-Net adopts an encoder-decoder architecture with skip connections. In the encoder, random sampling is used to reduce point cloud density, thereby minimizing memory and computational overhead. In the LFA module, an attention mechanism and dilated residual block are introduced to fully extract features. In the decoder, upsampling is achieved by k-nearest neighbor (KNN) and linear interpolation.

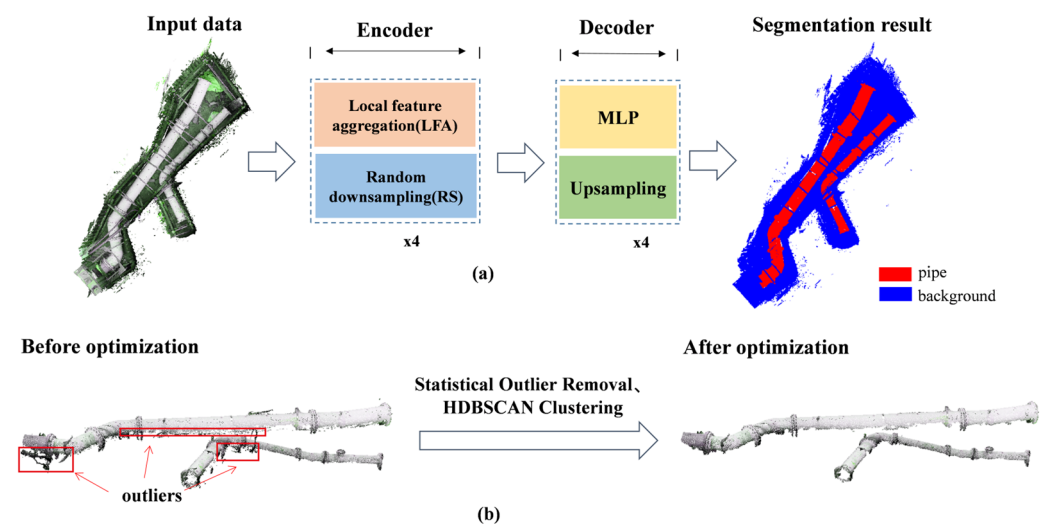


**Figure 2.** Data preprocessing. (a) Segmenting underground pipes from complex backgrounds based on RandLA-Net networks. (b) Optimization of segmentation results using HDBSCAN clustering and point cloud filtering algorithms to remove noise and outliers.

#### 3.1.2. Filtering and Optimization

The pipe points extracted from semantic segmentation still contain some noise and outliers, which are sparsely distributed. To address this, statistical filtering and the HDBSCAN (Hierarchical Density-Based Spatial Clustering of Applications with Noise) clustering are employed. Statistical filtering calculates the distance between each point and its neighboring points, statistically analyzes the distribution of these distances, and compares them with a predefined threshold (usually determined by the mean distance and standard deviation). Points exceeding this threshold are then removed, effectively targeting small-scale and scattered noise points. HDBSCAN constructs a density tree to form a clustering structure [38]. This method does not require pre-specifying the number of clusters and can automatically identify the optimal number of clusters, making it suitable for handling data with size

variations and a large amount of noise. The segmentation results before and after applying the filtering and optimization are shown in Figure 2b.

### 3.2. Extraction of Centerline Point Set

The centerline, also described as the skeleton, serves as an abstract representation of pipelines, reflecting both their geometric features and topological structures [29]. A pipe can be defined by its radius and centerline, along with the associated topological connections. In this study, the centerline of a pipe is initially extracted based on the Rotational Symmetry Axis (ROSA) method proposed by Tagliasacchi et al. [39]. This algorithm conceptualizes the pipe centerline as a generalized rotational symmetry axis, where centerline can be formed by connecting center points of several locally optimal cutting planes (ROSA points). Thus, extraction of the pipe centerline is transformed into searching for local optimal cutting planes and localization of ROSA points. Figure 3a presents an example of pipe data. To mitigate the impact of missing data, the ROSA algorithm incorporates compensation strategies using features derived from point normals.

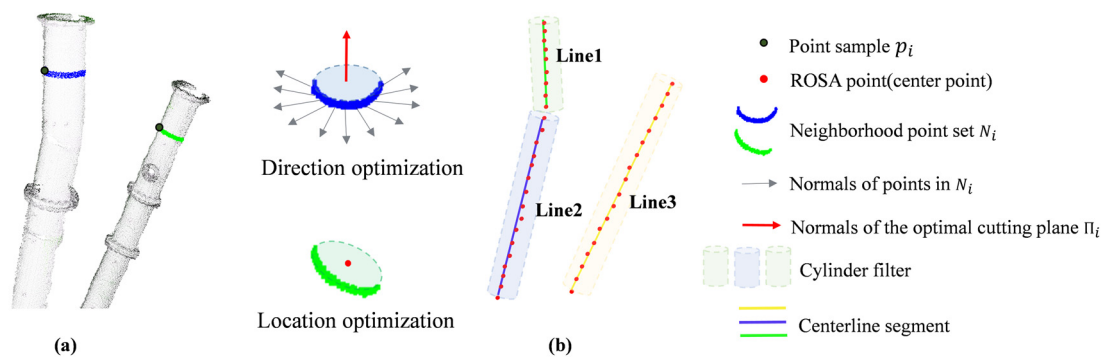


**Figure 3.** Overview of the methodology. (a) Preliminary extraction of pipe centerline. (b) Centerline segment fitting.

#### 3.2.1. Local Optimal Cutting Plane

A random sample point  $p_i$  is selected from pipe points, and its corresponding local optimal cutting plane  $\pi_i$ , which is perpendicular to the pipe's extension direction, can be determined. The center point of  $\pi_i$  is the ROSA point  $r_i$ , defined by coordinates  $x_i$  and normal vector  $v_i$ . The determination of  $\pi_i$  is performed iteratively. Starting from a randomly selected initial direction  $v_i^0$ , the normal vector  $v_i$  is iteratively optimized to update the cutting plane. In each iteration, the cutting plane  $\pi_i^j$  is determined based on  $p_i$  and the current normal  $v_i^j$ . The Mahalanobis distance, incorporating both Euclidean and directional space information, is used to derive current neighborhood points  $N_i^j$  for  $\pi_i^j$ , where  $j$  represents the number of direction iterations. The optimal normal  $v_i$  of  $r_i$  (i.e., the normal of  $\pi_i$ ) is the one minimizing sum of angular variance with normals of points in  $N_i$ , ensuring  $\pi_i$ 's normal is most rotationally symmetric with respect to normals of points in  $N_i$ . As shown in Figure 3a, black points represent randomly selected sample points  $p_i$ , blue and green bands represent the neighborhood point cloud  $N_i$  derived from  $\pi_i$ , gray arrows indicate normals of points in  $N_i$ , and red arrows indicate normal  $v_i$  of  $\pi_i$ . The sum of angular variation between  $v_i$  and normals of points in  $N_i$  should be minimized. Due to missing data,  $N_i$  is often incomplete, but this is compensated using point normals to preserve symmetry.

#### 3.2.2. Positioning of the ROSA Point

After determining the local optimal cutting plane  $\pi_i$ , the normal  $v_i$  of the ROSA point is also determined. Next, the position of the ROSA point is optimized. Given the optimal

cutting plane  $\pi_i$  and corresponding neighborhood  $N_i$ , the optimal position  $x_i$  of the ROSA point is determined by minimizing the sum of squared distances from  $x_i$  to the extensions of normals of points in the neighborhood  $N_i$ . The red point in Figure 3a represents the final position of the ROSA point. The optimization function is as follows:

$$x_i = \underset{x \in R^3}{\operatorname{argmin}} \sum_{p_j \in N_i} \|(x - p_j) \times n(p_j)\|^2, \quad (1)$$

where  $n(p_j)$  is the unit normal of point  $p_j$ . By solving the function, the position  $x_i$  of the ROSA point can be found. Since pipeline joints are usually non-cylindrical and lack a clear rotational symmetry axis, the Laplacian smoothing algorithm is used to ensure smooth connections between branches. Additionally, the moving least squares (MLS) method is applied for further refinement. Finally, the center of the joint is re-adjusted using Equation (1), resulting in the initial centerline point set  $C : \{c_i\}$ .

The radius of the pipe is calculated by the shortest distance from each center point  $c_i$  to surrounding pipe points. However, due to the presence of noise and outliers, the nearest point may not correspond to the correct point on the pipe surface, leading to errors. To mitigate the impact of noise, the k-nearest neighbor method is used, where the median of distances from  $c_i$  to the k points is taken as radius  $radii_i$ . Following the generation of initial centerline point set  $C : \{c_i\}$ , due to the disordered nature and the possibility of positional offsets, fitting and refinement of the centerline are necessary.

### 3.3. Centerline Generation

#### 3.3.1. Centerline Fitting

This study uses the RANSAC line fitting algorithm to process the initial centerline point set  $C$ . The classic RANSAC algorithm iteratively optimizes the fitting result by identifying inliers and outliers. At each iteration, the distances between data points and the fitted model are measured and compared against a predefined distance threshold. Points within the threshold are classified as inliers, while those outside are marked as outliers. By adjusting the threshold, the sensitivity of the model to noise and outliers can be controlled, which affects the accuracy of the final fitting result.

However, the RANSAC algorithm's inherent randomness makes it vulnerable to noisy data, increasing the risk of misfitting different line segments as a single line. To address this limitation, an improved RANSAC fitting method is proposed (Figure 3b). Specifically, after each RANSAC fitting, Density-Based Spatial Clustering of Application with Noise (DBSCAN) clustering is applied to process the remaining data points. This clustering step partitions the points into multiple subsets based on spatial proximity, allowing subsequent line fitting to be performed independently within each subset. Since points belonging to the same line segment are theoretically close in space, this data partition strategy effectively reduces the risk of misfitting.

To further suppress the false line segment problem caused by noisy points in  $C$ , this study adopts a parameter-adaptive adjustment strategy. It is known that noisy points in  $C$  are mostly located inside the pipe, with a denser distribution closer to the pipe centerline. The RANSAC algorithm is applied iteratively to generate candidate centerlines  $cl_i$  from  $C$ . The distance threshold for each fitting is set as  $\alpha \text{ Radii}$ , where  $\text{Radii}$  is the average radius of points in  $C$ , and  $(\alpha \in (0, 1))$  is an empirically set constant scalar. Next, with  $cl_i$  as the centerline and  $\beta \text{ Radii}$  as the radius, where  $(\beta \in (1, 2))$  is an empirically set constant scalar, a cylindrical neighborhood search is performed. The points found in the search are labeled as noisy points and removed from the initial point set  $C$ , preventing them from participating in subsequent fittings. Thus, the fitting parameters are dynamically adjusted based on the pipe radius, enhancing the algorithm's generalization ability in pipes of various sizes.

The final result is a candidate centerline set  $CL : \{cl_i\}$ , where each  $cl_i$  is defined by the centerline endpoints  $E_i = \{E_i^1, E_i^2\}$ , direction vector  $Dir_i$ , and radius  $R_i$ , with  $R_i$  being the average radius of the inlier points fitted.

### 3.3.2. Centerline Refinement

To prevent accuracy degradation caused by incorrect fitting and overfitting, this study introduces three indicators to optimize the fitting results. The first indicator is the angle between candidate centerlines. The second is the endpoint distance (ED), where  $ED_{ij}$  represents the shortest distance between the endpoints of two straight pipes. The third is the line distance (LD), where  $LD_{ij}$  represents the shortest distance from line  $cl_i$  to line  $cl_j$ , as shown in Figure 4.

$$ED_{ij} = \min(\text{dist}(E_i, E_j)), \quad (2)$$

$$LD_{ij} = \begin{cases} \frac{|v \cdot (Dir_i \times Dir_j)|}{\|Dir_i \times Dir_j\|}, & \|Dir_i \times Dir_j\| \neq 0 \\ \frac{\|v \times Dir_i\|}{\|Dir_i\|}, & \|Dir_i \times Dir_j\| = 0 \end{cases}, \quad (3)$$

where  $\text{dist}(E_i, E_j)$  calculates the distance matrix between endpoint pairs  $E_i$  and  $E_j$ ;  $v = E_i^1 - E_j^1$ , where  $v$  represents the relative displacement between the endpoints of the line segments.

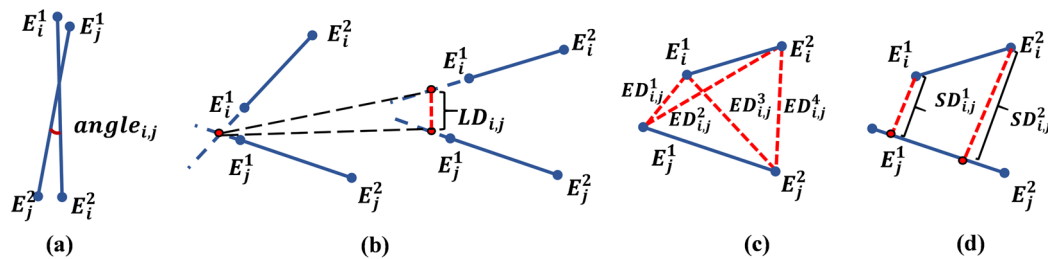


**Figure 4.** The indicators proposed, taking skew lines as an example. (a) Angle between lines. (b) Line distance. top view on the left, and side view on the right. (c) The minimum from  $ED_{i,j}^1$  to  $ED_{i,j}^4$  is the endpoint distance. (d) The minor between  $SD_{i,j}^1$  and  $SD_{i,j}^2$  is the segment distance from the  $i$ -th line to the  $j$ -th line.

The optimization strategy is based on angle and distance matching criteria to be implemented as follows:

$$K_m = \text{fit} \left( \left\{ cl_i \mid cl_i, cl_{max} \in CL, \text{angle}_{i,max} < \frac{\Pi}{12}, ED_{i,max} < \theta, LD_{i,max} < R_{max} \right\} \right), \quad (4)$$

where  $K_m = \{K_m^1, K_m^2\}$  represents the point pairs obtained by refinement, where  $m$  is the iteration number. The function  $\text{fit}()$  performs least squares fitting on all candidate line segments that meet the criteria and computes the endpoints.  $\theta$  is a pre-set constant and can be set to a relatively large value, as the centerline may be disconnected due to missing pipe data. The LD indicator ensures that even with a large  $\theta$  different parallel pipes will not be incorrectly connected. The algorithm is implemented iteratively. After each iteration, the line segments that meet the criteria are removed from  $CL$ , and the longest candidate line segment is added as the new seed, until all valid candidate line segments are processed.

### 3.4. Topological Reconstruction

Underground pipe components include straight pipes, elbows, and tees. Through the aforementioned steps, we obtained the key point set  $K = \{K_1, K_2, \dots, K_n\}$ , representing the positions of straight pipes. The information of elbows and tees can be determined by analyzing the topological connections between straight pipes (Figure 5). To achieve topological construction, this study introduces a new indicator, segment distance (SD).  $SD_{ij}$

represents the shortest distance from endpoints of the  $i$ -th straight pipe to the  $j$ -th straight pipe, and is calculated as follows:

$$SD_{ij} = \begin{cases} \min(\text{dist}(K_i, P_{ij})), & 0 < \vec{K}_j^1 K_j^2 \cdot \vec{K}_j^1 P_{ij} < \|\vec{K}_j^1 K_j^2\|^2, \\ \min(\text{dist}(K_i, K_j)), & \end{cases} \quad (5)$$

where  $P_{ij} = \text{proj}_{K_j^1 K_j^2}(K_i)$  is the projected point of  $K_i$  on line segment  $K_j^1 K_j^2$ .

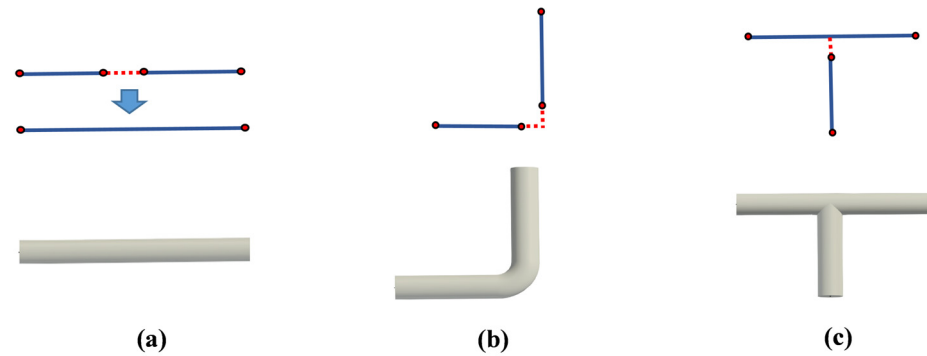


**Figure 5.** Topological reconstruction. (a) Collinear. (b) Elbow connection. (c) Tee connection. The blue lines represent the centerlines of individual pipes, and the red dots represent the endpoints.

By combining the SD and ED proposed in Section 3.3.2, the connection type between straight pipes is determined. If the ratio of ED to SD exceeds a preset threshold, indicating the SD between straight pipes is small but the ED is large, the connection is classified as a tee, with the  $i$ -th straight pipe as the branch pipe and the  $j$ -th straight pipe as the main pipe. If both the SD and ED are small, the connection is classified as an elbow. The classification of these three connection types is shown in Figure 5. The parameter extraction results (radius and centerline with topological connections) are integrated to realize BIM reconstruction of the pipeline. The final model is created in Revit with Dynamo.

### 3.5. Accuracy Evaluation

To evaluate the performance of the proposed framework, accuracy assessment from multiple perspectives is conducted. At the object level, the framework's ability to detect pipeline components is assessed using precision and recall metrics. Precision is used to measure the proportion of true pipe components among the components detected. Recall is used to measure the proportion of pipe components correctly detected among the true components. From a point-level perspective, the deviation analysis method proposed by Anil et al. [40] for BIM quality evaluation was adopted. The nearest distance from each point to the reconstructed model is calculated as a measure of similarity, which can reflect both the overall fitting effect, as well as identifying areas with poor local fitting. The deviation threshold of 0.15 m set in this study is an empirically determined parameter, designed to effectively excludes local errors, while concurrently providing an accurate representation of the overall alignment between the model and the actual point cloud data [15]. Points with deviations exceeding this threshold were considered noise or irrelevant objects that were not modeled. These points were excluded from further analysis to minimize the impact of noise on accuracy metrics. Additionally, three metrics—mean absolute error (MAE), root mean square error (RMSE), and relative mean error (MRE)—were used to measure the error in pipe radius, as shown in the following formulas:

$$MAE = \frac{1}{m} \sum_{i=1}^m |R_i - \hat{R}_i|, \quad (6)$$

$$RMSE = \sqrt{\frac{1}{m} \sum_{i=1}^m (R_i - \hat{R}_i)^2}, \quad (7)$$

$$MRE = \frac{1}{m} \sum_{i=1}^m \frac{|R_i - \hat{R}_i|}{\hat{R}_i}, \quad (8)$$

where  $R_i$  is the true radius of the  $i$ -th pipe, obtained through manual measurements and verified with design documents, and  $\hat{R}_i$  is the estimated radius, with  $m$  representing the number of samples.

## 4. Results

### 4.1. Visualization of BIM Result

Figure 6 shows the reconstruction results tested on three actual scan datasets, showcasing three scenes from top to bottom. From left to right, each row presents: input scene point cloud data, extracted pipeline points after preprocessing, and the reconstructed BIM model. The accuracy of pipeline points, derived through semantic segmentation, is shown in Table 2, demonstrating the high performance.

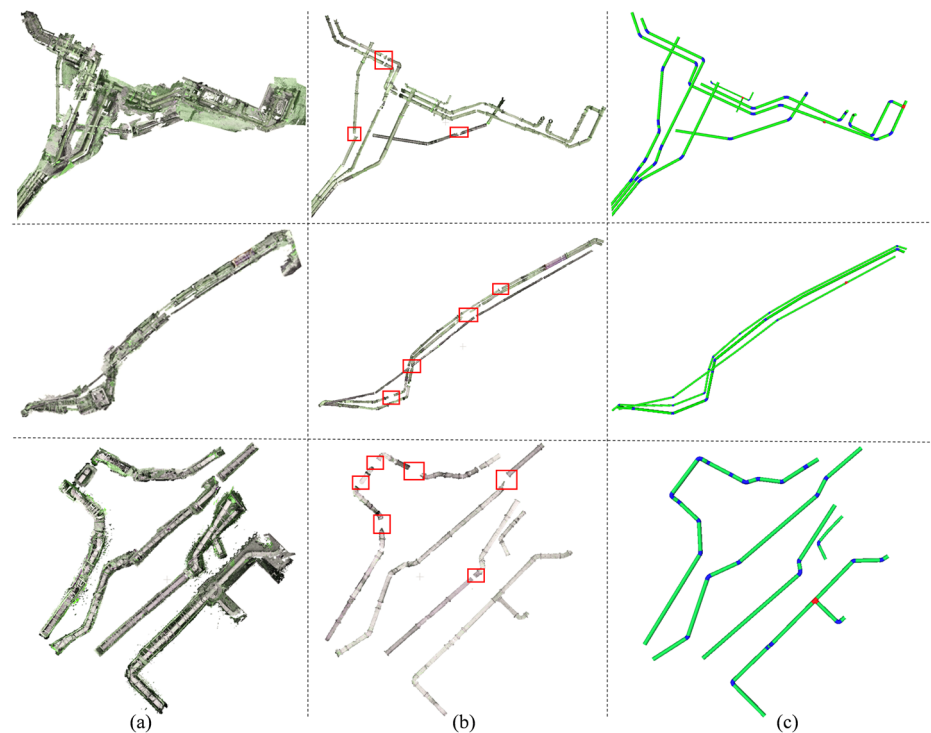


**Figure 6.** Processing results. From top to bottom: Scene A, Scene B, and Scene C. From left to right: (a) scanned point cloud with RGB coloring, (b) pipe points after preprocessing (missing parts of pipe are marked with red boxes), and (c) pipe BIM model. In the third column, green represents straight tubes, blue represents elbows, and red represents tee tubes.

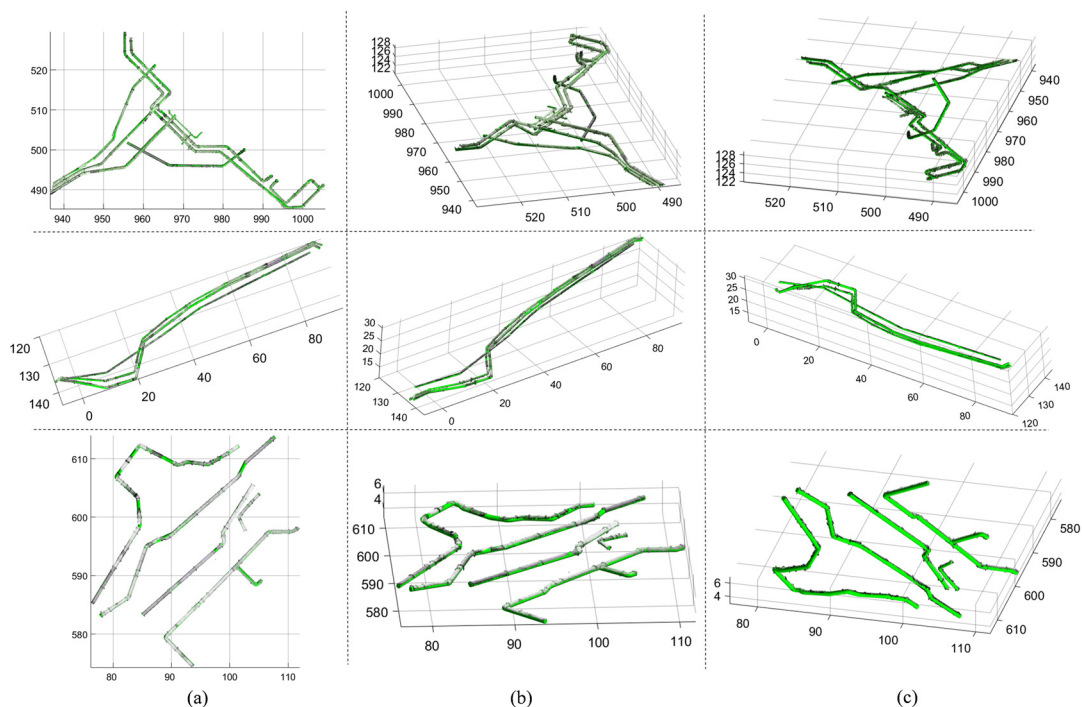
**Table 2.** Accuracy assessment of semantic segmentation.

	Precision	Recall	F1 Score	IOU	mIOU	OA
Pipe	0.861	0.872	0.866	0.764	0.859	0.959
Non-pipe	0.977	0.975	0.976	0.953		

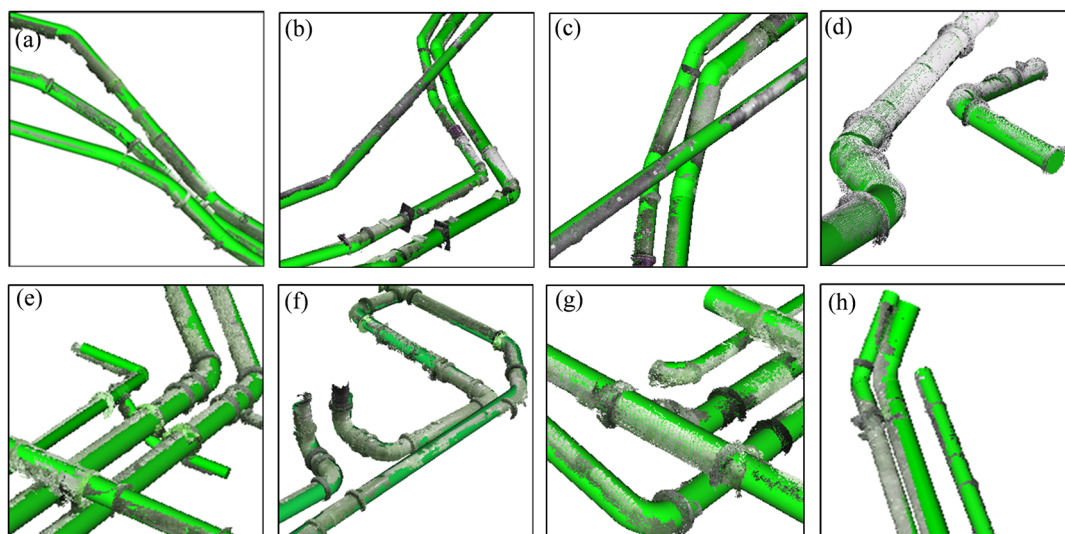
Scene A features a high-density background, occupying a significant portion of the scene, and a complex pipe structure with multiple branches and interwoven distribution. The extracted pipe points contain missing and broken sections, which are highlighted in red boxes in Figure 6b. These gaps are mainly due to scanning occlusions or limited viewpoints. As shown in Figure 6c, missing sections are connected through structural analysis, and the multi-branch structure is effectively restored, closely resembling the real distribution. Scene B has a relatively simple background but still contains a high density of discrete noise points, likely caused by laser scattering through particles such as dust or smoke in the air. The extracted pipes mainly extend in the same direction, forming an alternating or array-like pattern. Despite missing and broken sections, the reconstructed BIM model effectively restores the pipe's overall structure by connecting these gaps. Compared to the previous two scenes, Scene C benefits from a simple background and high-quality data. The extracted pipes extend in various directions and forms with a relatively simple structure, showing no significant overlaps. While missing sections in the pipe point cloud are noticeable, the BIM reconstruction successfully achieves a complete representation of the pipe distribution.

Figure 7 offers a multi-perspective view of the results, displaying pipe points overlaid on the BIM model from three angles: top-down, 45° downward, and 45° upward. This multi-perspective presentation effectively reveals the spatial layout and vertical distribution features of pipes. In the top-down view (Figure 7a), the overall XOY plane distribution of pipes is clearly visible. Scene A demonstrates a dense, multi-branch, interwoven structure, while Scene B shows pipes extending in a main direction with a regular layout. Scene C presents a simpler structure with multi-directional extensions and minimal overlaps. The overlay of point cloud and BIM shows that the reconstructed BIM closely aligns with the planar distribution of the pipe points, achieving high accuracy in the XOY plane. In the 45° downward view (Figure 7b), the vertical structure and depth variations of pipes are revealed. It is evident that in Scenes A and B the pipes show significant fluctuations in vertical direction. Scene A features multiple pipe segments at varying depths, reflecting a high degree of vertical complexity, whereas Scene B displays inclined extensions. Scene C, despite its diverse forms, has a relatively simple vertical structure. The reconstructed BIM aligns well with the vertical distribution of point cloud and effectively restores short pipe segments with slopes, validating the proposed method's adaptability to multi-level spatial structures. In the 45° upward view (Figure 7c), the lower structure and slope features of pipes are highlighted. Overall, the results from different perspectives further validate the accuracy and robustness of the proposed framework, especially its strong reconstruction capability for complex pipe structures with slopes. This multi-perspective verification shows that the method can adapt to the multi-angle and multi-level features in complex scenes, thereby meeting the practical requirements for 3D reconstruction of underground pipes.

Figure 8 provides close-up views of critical areas with slope variations and dense pipe arrangements, presenting the alignment of BIM and pipe points from a side perspective. In the slope variation area (e.g., Figure 8a–d), pipes show the up-and-down undulation and inclined distribution, which are accurately captured by the BIM model. In areas with dense pipe arrangements (e.g., Figure 8e–h), multiple pipes intersect and overlap, forming a complex structure that is prone to occlusion. The reconstructed model effectively restores the relative positions and orientations of the pipes in these regions. Overall, these detailed local views validate the proposed method's capability to reconstruct complex structures and recover critical features, ensuring applicability in challenging reconstruction scenarios.



**Figure 7.** Pipe points (RGB coloring) superimposed on the BIM model (green). From top to bottom: Scene A, Scene B, and Scene C. From left to right: (a) top-down view, (b) 45° downward view, and (c) 45° view from below. The axes on the graph are measured in meters.



**Figure 8.** Close-up views of pipe points (RGB coloring) superimposed on the BIM model (green). (a–d) Slope variation areas. (e–h) Areas with dense pipe arrangements.

#### 4.2. Accuracy Analysis

Table 3 summarizes the quantitative evaluation of reconstruction accuracy across three real-world scenes. The centerline fitting and refinement methods used in this study achieve high-quality results. The modeling for straight pipes, elbows, and tees shows overall high detection accuracy. Scene A yields the most favorable results for straight pipes, with 42 out of 45 correctly reconstructed. This corresponds to a recall rate of 93.3% and a precision rate of 95.5%, indicating minimal false positives. For elbows, the algorithm demonstrates a precision rate of 97.0%, reflecting a low rate of misclassification, but the recall rate of 84.2% suggests some undetected elbows. Tees occupy a small proportion of the scene, with a recall rate of only 50.0%, indicating challenges in detecting tees in more complex

distributions. Scene B, characterized by lower complexity than Scene A, poses challenges in reconstructing small-slope short pipes. Straight pipes in this scene achieve a recall rate of 88.0% and a precision rate of 91.7%, reflecting slightly lower performance compared to Scene A. For elbows, the recall rate is 81.8%, and the precision rate is 90.0%. These results suggest that variations in scene complexity and data features can impact reconstruction accuracy. Scene C demonstrates excellent accuracy, particularly for straight pipes, achieving a recall rate of 94.1% and a precision rate of 100.0%, indicating highly accurate detection with no false positives. Elbow detection is similarly strong, with both recall and precision rates reaching 92.9% and 100.0%, respectively. Across all scenes, the reconstruction results exhibit high precision for all different components, indicating that our approach has almost no misclassification because noise removal optimization is performed based on the pipe segmentation results. The recall rate of pipe components is a more important indicator of whether the framework can detect and reconstruct pipe components comprehensively and accurately. The experimental results demonstrate that the method maintains a high recall rate in complex environments, showing excellent detection performance and consistent efficiency in real-world application scenes.

**Table 3.** Accuracy analysis for pipe components.

			Scene A					Scene B					Scene C		
	AP <sup>1</sup>	RP <sup>2</sup>	TP <sup>3</sup>	Recall	Precision	AP <sup>1</sup>	RP <sup>2</sup>	TP <sup>3</sup>	Recall	Precision	AP <sup>1</sup>	RP <sup>2</sup>	TP <sup>3</sup>	Recall	Precision
line	45	44	42	93.3	95.5	25	24	22	88.0	91.7	34	32	32	94.1	100.0
elbow	38	33	32	84.2	97.0	22	20	18	81.8	90.0	28	26	26	92.9	100.0
tee	4	2	2	50.0	100.0	0	1	0	/	0.0	1	1	1	100.0	100.0
total	87	79	76	87.4	96.2	47	44	40	85.1	90.9	63	59	59	93.7	100.0

<sup>1</sup> AP denotes actual pipe (units: number). <sup>2</sup> RP denotes reconstructed pipe (units: number). <sup>3</sup> TP denotes true positive pipe (units: number).

#### 4.3. Deviation Analysis

Figure 9 shows the deviation analysis results, comparing the reconstructed models with the pipe points data. Figure 9a is a color-coded deviation map, where the gradient from blue to red corresponds to deviation values ranging from  $-0.15$  m to  $0.15$  m. Points with accurate reconstruction are predominantly green, indicating minimal deviation. Figure 9b is a histogram showing the statistical distribution of deviations after removing points with deviations greater than  $0.15$  m. The x-axis represents the deviation values, and the y-axis represents the proportion of points at each deviation value. The histogram shows that in Scene A nearly 75% of the point cloud data has a deviation between  $-0.05$  m and  $0.05$  m. However, some points with deviation values between  $0.05$  m and  $0.15$  m indicate that the overall model fitting is good, but there are large localized deviations. Affected by short pipes with slopes, Scene B has about 60% of points with deviations less than  $0.05$  m, slightly lower than Scene A. In Scene C, over 80% of points have deviations less than  $0.05$  m, indicating high reconstruction accuracy. Overall, the deviations in all three scenes generally follow a normal distribution, with RMSE values across all three scenes below 6 cm. The proposed method achieves high overall reconstruction accuracy, with deviations mainly concentrated within an acceptable range.

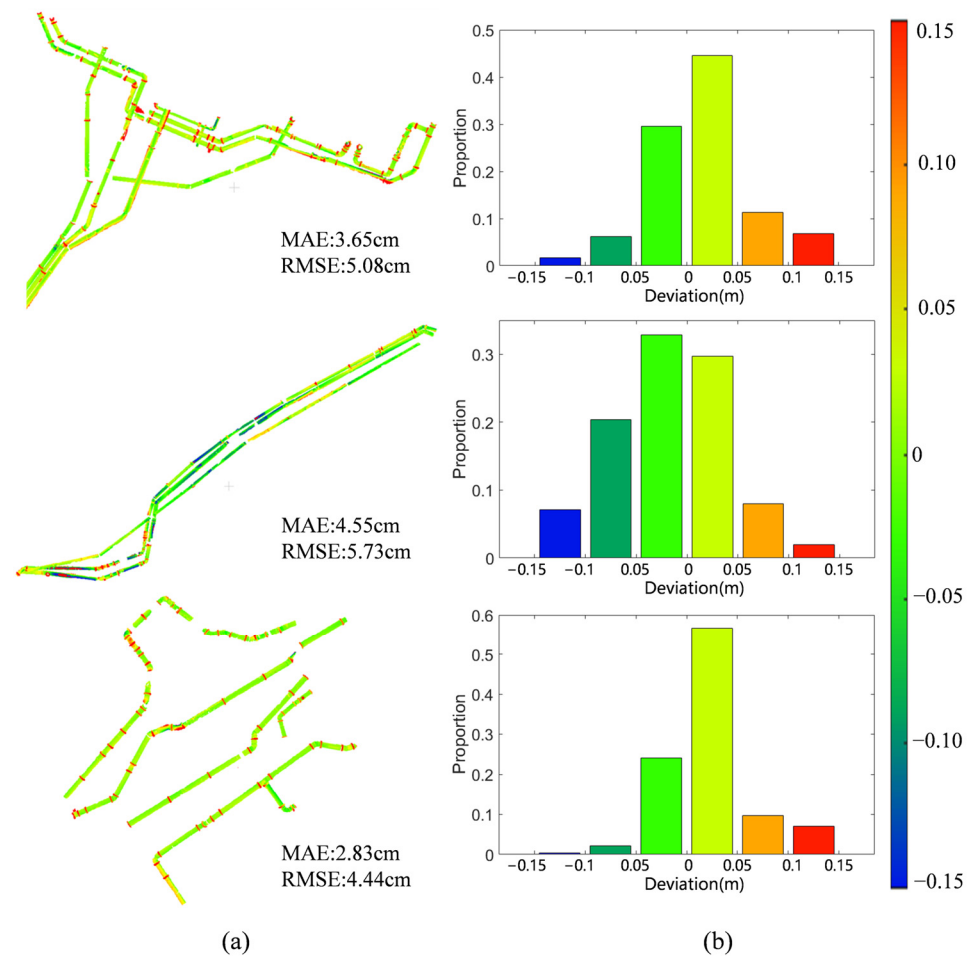


**Figure 9.** Deviation analysis of pipe points to reconstructed BIM models in different scenes. From top to bottom: Scene A, Scene B, and Scene C. (a) Deviation maps with a threshold of 0.15 m, where the color of points corresponds to deviation values ranging from  $-0.15$  m to  $0.15$  m, transitioning from blue to red. (b) Deviation histograms of pipe points.

#### 4.4. Analysis of Errors in Pipe Radius

The error distribution of pipe radius for Scenes A, B, and C is shown in Figure 10. The statistical results indicate that 79.0% of pipes in Scene A, 72.4% in Scene B, and 79.1% in Scene C have radius estimation errors less than 10 mm, demonstrating the high accuracy of the proposed method in extracting pipe radii. Quantitative analysis reveals that the mean error for Scene A is 7.15 mm, the root mean square error (RMSE) is 7.87 mm, and the average relative error is 2.60%. In Scene B, affected by noisy points, the highest mean error of 8.55 mm and RMSE of 8.72 mm were observed, reflecting the challenges posed by data quality. However, the average relative error remained relatively low at 2.54%, demonstrating the robustness of our method even under less-than-ideal conditions. Scene C showed the best performance, with a mean error of 6.42 mm, RMSE of 6.86 mm, and average relative error of 2.22%. Overall, the average relative errors for all scenes are below 3%, verifying the reliability and stability of the proposed method under various conditions.

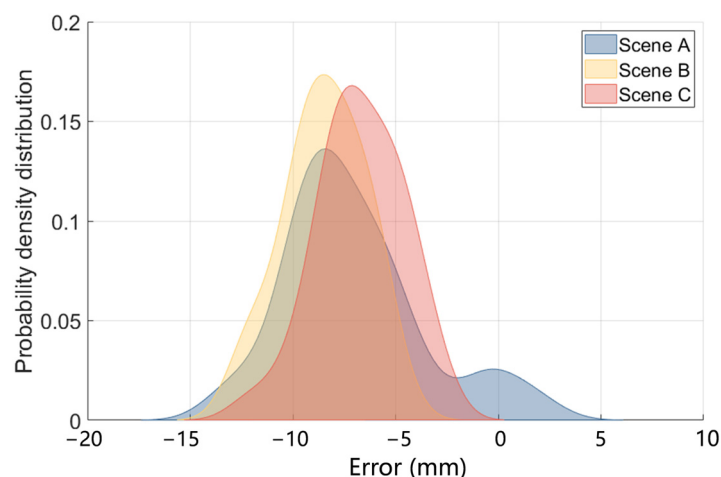


**Figure 10.** Deviation analysis of pipe points to reconstructed BIM models in different scenes.

#### 4.5. Experimental Verification

##### 4.5.1. Comparative Experiment

To demonstrate the advantages of the ROSA-based centerline extraction approach, a comparison is conducted with the L1-medial skeleton method [41] and the Laplacian-based contraction (LBC) algorithm [42], using Scene B as the test case. The L1-medial skeleton method employs iterative optimization to identify the points minimizing the total absolute distance as the L1-median, thereby extracting the skeleton structure. Cao et al. [42] utilized a Laplacian operator for the contraction of point clouds, applying local Delaunay triangulation and topological refinement to iteratively extract the curve skeleton.

Figure 11 illustrates the performance of three skeleton extraction methods: ROSA, L1-median, and LBC. In this study, ROSA is the primary method employed. The results indicate that skeletons extracted by ROSA (Figure 11a) and LBC (Figure 11c) exhibit cleaner structures with fewer noise points, whereas those obtained via the L1-median method show a significantly higher degree of noise and larger deviations (Figure 11b). To quantify the accuracy of skeleton extraction, the mean absolute error (MAE) is calculated, representing the difference between estimated pipe radius based on skeleton points and the true value (with a ground truth radius of 0.3 m in Scene B). ROSA achieves an exceptional MAE of 0.855 cm, demonstrating high accuracy in skeleton positioning. In contrast, the MAEs of LBC and L1-median are 2.729 cm and 3.261 cm, respectively, indicating larger errors in their results.

The displacement of skeleton points in the LBC and L1-median methods can be primarily attributed to the significant data missing in the pipe points, which is a common challenge in point cloud processing. Therefore, the ROSA method emerges as the most accurate for pipe skeleton extraction. Its robust performance further substantiates its superiority in extracting reliable centerlines from point cloud data.

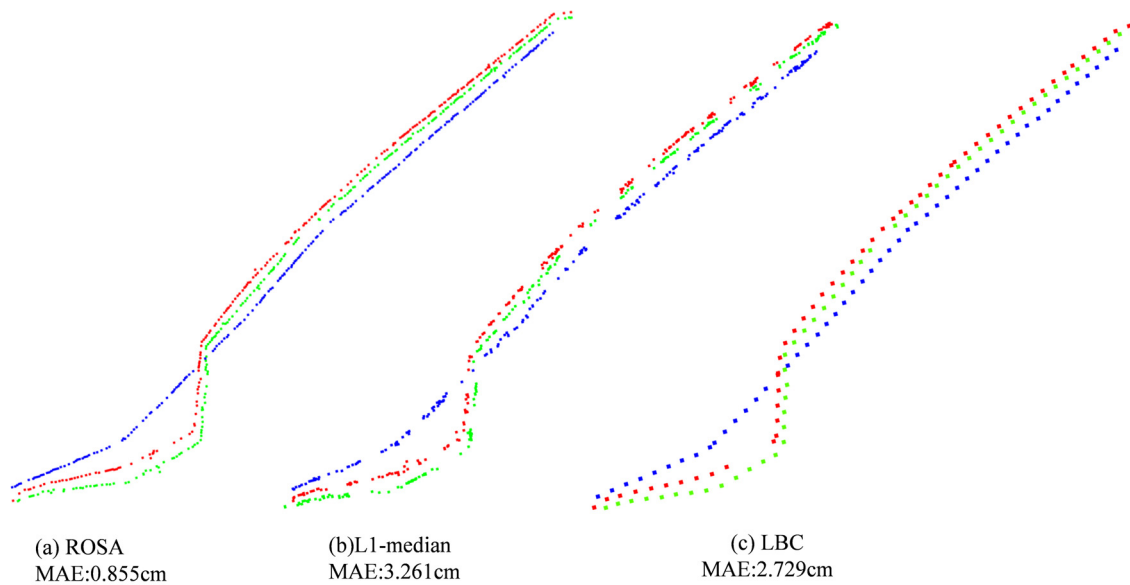


**Figure 11.** Visual comparison of skeleton extraction results: (a) ROSA method, (b) L1-median method, and (c) LBC method. The different colors represent the skeleton points of different pipes.

#### 4.5.2. Ablation Experiment

An ablation experiment was conducted using data from Scene A to evaluate the effectiveness of the proposed improved RANSAC and centerline refinement method. Figure 12a shows the fitting results based on only the classical RANSAC method, while Figure 12b presents the results after applying the improved RANSAC method.

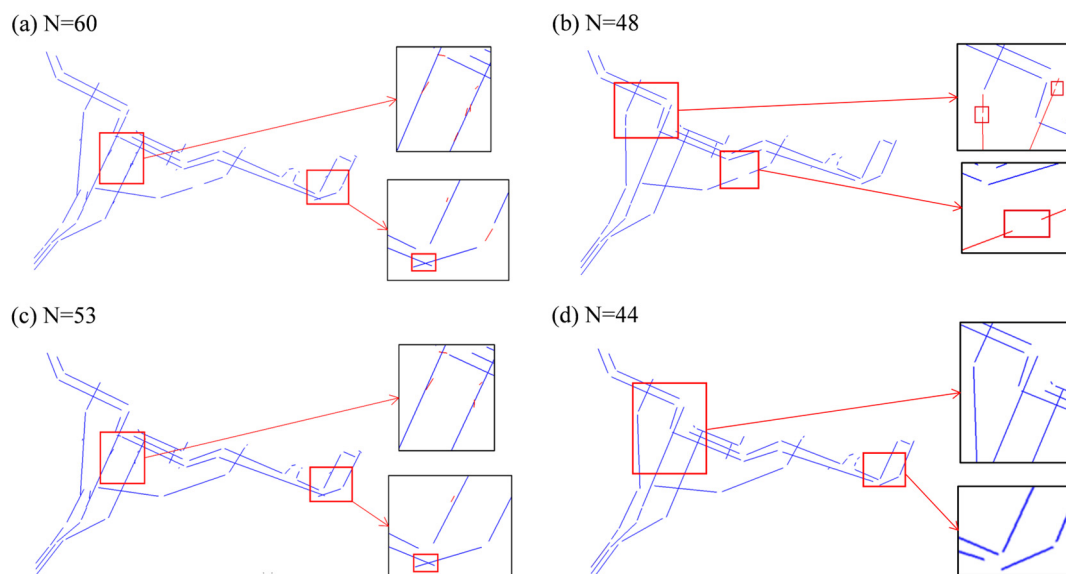


**Figure 12.** Centerline fitting results. (a) The classical RANSAC algorithm. (b) The improved RANSAC algorithm. (c) The classical RANSAC algorithm and keypoint refinement. (d) The improved RANSAC algorithm and keypoint refinement. The zoomed-in areas show the centerlines: blue lines represent the correct centerline, and red lines represent the incorrect lines.

A comparison between figures highlights two primary sources of error in Figure 12a: (1) the generation of false short segments, and (2) the fitted line segments deviating from the actual ones. These issues are primarily attributed to the noise present in the initial centerline point set. In contrast, the improved RANSAC algorithm, as shown in Figure 12b, significantly mitigates these problems, with most spurious short segments eliminated.

However, some errors persist, including instances where a single line segment is incorrectly divided into multiple segments. The proposed centerline refinement method effectively addresses this issue. Figure 12c illustrates the results of applying the refinement method independently, showing that it effectively removes some of the short segments and reduces the number of errors, as evidenced by the improvements within the red box. Finally, Figure 12d depicts the optimal results achieved by applying both the improved RANSAC algorithm and the centerline refinement method. According to the statistical results, as the methods proposed in this study were progressively applied, the number of fitted line segments decreased from 60 to 44, indicating a substantial reduction in spurious line segments and an improvement in overall fitting accuracy.

#### 4.6. Processing Time

Table 4 summarizes the processing times for the proposed method across three distinct scenes. The total processing times for Scene A, Scene B, and Scene C are 13.24, 8.12, and 3.02 min, respectively. In contrast, traditional modeling methods, depending on the experience of modelers and the scale and complexity of scenes, typically require several days or even months to complete. The proposed method significantly reduces the time required for data processing, and the model generation also decreases reliance on highly skilled manual operations, thereby resulting in considerable reductions in labor costs. Additionally, this method minimizes measurement and modeling errors commonly introduced by manual operations, leading to improvements in both the accuracy and consistency of generated models.

**Table 4.** Processing time of the underground pipe data.

	Filtering and Optimization	Parameter Extraction	Model Reconstruction	Total
Scene A	4.80 min	8.14 min	0.30 min	13.24 min
Scene B	2.30 min	5.61 min	0.21 min	8.12 min
Scene C	1.38 min	1.43 min	0.21 min	3.02 min

## 5. Discussion

This study proposes a BIM reconstruction framework for underground pipeline systems based on laser point clouds. Given the prevalent challenges of missing and sparse point cloud data, achieving high-precision and fully connected BIMs has remained elusive in prior research. Many existing methods for 3D reconstruction face notable limitations. For instance, some approaches require pipe orientations to align with the main axes [25], fail to reconstruct the topological relationships between pipes [22,35], or involve complex parameter settings [23]. Moreover, most research has focused on pipeline systems in open environments, such as industrial plants or mechanical, electrical, and plumbing (MEP) systems. These methods are often unsuitable for the unique complexities of underground environments, making their direct application to BIM reconstruction of underground pipelines challenging. To address these issues, this study proposes a high-precision centerline generation and topological reconstruction framework, which effectively mitigates the influence of residual noise in pipe points and enables the topological connection between disconnected pipes.

To validate the effectiveness of the proposed framework, actual point cloud data with varying complexity were tested. Experimental results demonstrated its high efficiency and robustness across all test scenes, achieving an overall recall rate of 88.8% and a precision rate of 96.2%. These metrics highlight the framework's superior performance and practical applicability in real-world scenes.

Despite achieving remarkable results, this study has some limitations. Firstly, the performance of the RandLA-Net semantic segmentation network may be suboptimal in highly complex scenes, particularly when there is substantial noise or when the distinction between pipes and the surrounding background is minimal. Given that the primary focus of this study is on the structural reconstruction of pipelines, optimization strategies were employed to enhance segmentation performance. However, to address the challenges posed by more complex underground environments, future research will seek to enhance segmentation accuracy by redesigning the segmentation architecture and benchmarking it against advanced, state-of-the-art semantic segmentation networks.

Next, while the framework is designed for underground pipelines, it does not address other common components in underground utility systems, such as valves and manholes. The reconstruction of these irregularly shaped components poses challenges for geometric-based methods. We will consider further exploring the automatic detection and reconstruction of these complex components based on template matching or deep learning algorithms. Enhancing the framework with these capabilities would further enhance its practicality and expand its application range in BIM reconstruction of underground utility systems.

## 6. Conclusions

This paper presents a framework for topological reconstruction of underground pipelines based on laser point clouds. Given the complex structure of underground pipelines and the issues of self-occlusion or occlusion by surrounding objects, the comprehensive framework which integrates a series of processes, including data preprocessing, the extraction of initial point sets for pipe centerlines, radius estimation, centerline generation, and topology reconstruction, is developed to achieve a high-precision BIM representation. Among these, centerline generation is a critical module of this framework. However, compared to above-ground scenes, an underground point cloud typically contains more intricate background noise, which can persist even after pipe segmentation and lead to inaccuracies in centerline determination. To address this, a centerline fitting and refinement approach is developed, significantly improving the modeling accuracy.

The framework is validated using real-world data from Hong Kong, successfully detecting and modeling 175 out of 197 components, including structures such as pipes, elbows, and tees. The framework achieves an overall recall rate of 88.8%, demonstrating its ability to effectively model most components. Deviation analysis reveals that the mean distance between pipe points and the reconstructed model is approximately 3.79 cm, indicating a strong geometric match between them. The mean relative errors in pipe radius estimation across three scenes were 2.60%, 2.54%, and 2.22%, respectively, all below 3%, confirming the high accuracy of parameter extraction. Additionally, the ablation experiment demonstrates that the improved RANSAC and centerline refinement method play crucial roles in enhancing the quality of centerline generation results.

In conclusion, the proposed framework provides a robust technical foundation for the management of underground pipeline systems in the context of smart city development. By facilitating the digitalization and intelligent management of urban infrastructure, this framework supports the operational efficiency and sustainable development of urban environments.

**Author Contributions:** Conceptualization, Q.L. and Q.X.; methodology, Q.L.; software, Q.L.; validation, Q.L., Y.L. and X.C.; formal analysis, Q.L.; investigation, Q.L.; resources, Q.X.; data curation, Q.L. and Y.L.; writing—original draft preparation, Q.L.; writing—review and editing, Q.L., R.W., Y.T. and Q.X.; visualization, Q.L.; supervision, Q.X. and R.W.; project administration, Q.X.; funding acquisition, Q.X. All authors have read and agreed to the published version of the manuscript.

**Funding:** This research was funded by National Natural Science Foundation of China (grant No. 42371483), National Natural Science Foundation of China (grant No. 42401573), the Postdoctoral Fellowship Program of CPSF (grant No. GZB20240880), and the project of ‘Underground Utilities Recognition and Extraction Service Based on Deep Learning of Point Cloud’ (No. GHK(2022)K003B01).

**Data Availability Statement:** The data presented are available on request from the corresponding author. The data are not publicly available due to privacy restrictions.

**Conflicts of Interest:** The authors declare no conflicts of interest.

## References

1. Li, Y.P.; Wang, N.N.; Lei, J.W.; Wang, F.M.; Li, C. Modeling GPR Wave Propagation in Complex Underground Structures Using Conformal ADI-FDTD Algorithm. *Appl. Sci.* **2022**, *12*, 5219. [[CrossRef](#)]
2. Xu, H.W.; Zhang, Q.Z.; Li, X.C. Based on 3D Technology Application Research about Urban Underground Pipeline Management Information System. In Proceedings of the International Conference on Applied Mechanics and Mechanical Engineering, Changsha, China, 8–9 September 2010; pp. 2227–2232.
3. Li, M.H.; Feng, X.; Han, Y.; Liu, X.D. Mobile augmented reality-based visualization framework for lifecycle O&M support of urban underground pipe networks. *Tunn. Undergr. Space Technol.* **2023**, *136*, 105069. [[CrossRef](#)]
4. Alreshidi, E.; Mourshed, M.; Rezgui, Y. Factors for effective BIM governance. *J. Build. Eng.* **2017**, *10*, 89–101. [[CrossRef](#)]
5. Condotta, M.; Scanagatta, C. BIM-based method to inform operation and maintenance phases through a simplified procedure. *J. Build. Eng.* **2023**, *65*, 105730. [[CrossRef](#)]
6. Veldhuis, H.; Vosselman, G. The 3D reconstruction of straight and curved pipes using digital line photogrammetry. *ISPRS J. Photogramm. Remote Sens.* **1998**, *53*, 6–16. [[CrossRef](#)]
7. Liu, J.P.; Fu, L.H.; Cheng, G.Z.; Li, D.S.; Zhou, J.; Cui, N.; Chen, Y.F. Automated BIM Reconstruction of Full-Scale Complex Tubular Engineering Structures Using Terrestrial Laser Scanning. *Remote Sens.* **2022**, *14*, 1659. [[CrossRef](#)]
8. Yang, F.; Pan, Y.T.; Zhang, F.S.; Feng, F.Y.; Liu, Z.J.; Zhang, J.Y.; Liu, Y.; Li, L. Geometry and Topology Reconstruction of BIM Wall Objects from Photogrammetric Meshes and Laser Point Clouds. *Remote Sens.* **2023**, *15*, 2856. [[CrossRef](#)]
9. Yang, L.; Zhang, F.S.; Yang, F.; Qian, P.; Wang, Q.K.; Wu, Y.J.; Wang, K.L. Generating Topologically Consistent BIM Models of Utility Tunnels from Point Clouds. *Sensors* **2023**, *23*, 6503. [[CrossRef](#)]
10. Cheng, G.Z.; Liu, J.P.; Li, D.S.; Chen, Y.F. Semi-Automated BIM Reconstruction of Full-Scale Space Frames with Spherical and Cylindrical Components Based on Terrestrial Laser Scanning. *Remote Sens.* **2023**, *15*, 2806. [[CrossRef](#)]
11. Wang, Q.; Kim, M.K. Applications of 3D point cloud data in the construction industry: A fifteen-year review from 2004 to 2018. *Adv. Eng. Inform.* **2019**, *39*, 306–319. [[CrossRef](#)]
12. Xu, Y.S.; Stilla, U. Toward Building and Civil Infrastructure Reconstruction From Point Clouds: A Review on Data and Key Techniques. *IEEE J. Sel. Top. Appl. Earth Obs. Remote Sens.* **2021**, *14*, 2857–2885. [[CrossRef](#)]
13. Bosché, F.; Ahmed, M.; Turkan, Y.; Haas, C.T.; Haas, R. The value of integrating Scan-to-BIM and Scan-vs-BIM techniques for construction monitoring using laser scanning and BIM: The case of cylindrical MEP components. *Autom. Constr.* **2015**, *49*, 201–213. [[CrossRef](#)]
14. Agapaki, E.; Brilakis, I. State-of-Practice on As-Is Modelling of Industrial Facilities. In Proceedings of the 25th Workshop of the European-Group-for-Intelligent-Computing-in-Engineering (EG-ICE), Lausanne, Switzerland, 10–13 June 2018; pp. 103–124.
15. Wang, B.Y.; Yin, C.; Luo, H.; Cheng, J.C.P.; Wang, Q. Fully automated generation of parametric BIM for MEP scenes based on terrestrial laser scanning data. *Autom. Constr.* **2021**, *125*, 103615. [[CrossRef](#)]
16. Kawashima, K.; Kanai, S.; Date, H. As-built modeling of piping system from terrestrial laser-scanned point clouds using normal-based region growing. *J. Comput. Des. Eng.* **2014**, *1*, 14. [[CrossRef](#)]
17. Xie, Y.; Li, S.Y.; Liu, T.R.; Cai, Y.Y. As-built BIM reconstruction of piping systems using PipeNet. *Autom. Constr.* **2023**, *147*, 104735. [[CrossRef](#)]
18. Xie, Y.; Teo, M.X.; Li, S.Y.; Huang, L.H.; Liang, N.Y.; Cai, Y.Y. As-built BIM reconstruction of piping systems using smartphone videogrammetry and terrestrial laser scanning. *Autom. Constr.* **2023**, *156*, 105120. [[CrossRef](#)]
19. Fischler, M.A.; Bolles, R.C. Random sample consensus: A paradigm for model fitting with applications to image analysis and automated cartography. *Commun. ACM* **1981**, *24*, 381–395. [[CrossRef](#)]
20. Tran, T.T.; Cao, V.T.; Laurendeau, D. Extraction of cylinders and estimation of their parameters from point clouds. *Comput. Graph.* **2015**, *46*, 345–357. [[CrossRef](#)]
21. Honti, R.; Erdélyi, J.; Kopáčík, A. Semi-Automated Segmentation of Geometric Shapes from Point Clouds. *Remote Sens.* **2022**, *14*, 4591. [[CrossRef](#)]
22. Liu, Y.J.; Zhang, J.B.; Hou, J.C.; Ren, J.C.; Tang, W.Q. Cylinder Detection in Large-Scale Point Cloud of Pipeline Plant. *IEEE Trans. Vis. Comput. Graph.* **2013**, *19*, 1700–1707. [[CrossRef](#)]

23. Jin, Y.H.; Lee, W.H. Fast Cylinder Shape Matching Using Random Sample Consensus in Large Scale Point Cloud. *Appl. Sci.* **2019**, *9*, 974. [[CrossRef](#)]
24. Li, M.H.; Feng, X.; Hu, Q.F. 3D laser point cloud-based geometric digital twin for condition assessment of large diameter pipelines. *Tunn. Undergr. Space Technol.* **2023**, *142*, 105430. [[CrossRef](#)]
25. Ahmed, M.F.; Haas, C.T.; Haas, R. Automatic Detection of Cylindrical Objects in Built Facilities. *J. Comput. Civ. Eng.* **2014**, *28*, 04014009. [[CrossRef](#)]
26. Figueiredo, R.; Moreno, P.; Bernardino, A. Robust cylinder detection and pose estimation using 3D point cloud information. In Proceedings of the 17th IEEE International Conference on Autonomous Robot Systems and Competitions (ICARSC), Univ Coimbra, Coimbra, Portugal, 26–28 April 2017; pp. 234–239.
27. Patil, A.K.; Holi, P.; Lee, S.K.; Chai, Y.H. An adaptive approach for the reconstruction and modeling of as-built 3D pipelines from point clouds. *Autom. Constr.* **2017**, *75*, 65–78. [[CrossRef](#)]
28. Rabhani, T.; Van Den Heuvel, F. Efficient hough transform for automatic detection of cylinders in point clouds. *ISPRS Workshop Laser Scanning* **2005**, *3*, 6.
29. Svensson, S.; Nyström, I.; di Baja, G.S. Curve skeletonization of surface-like objects in 3D images guided by voxel classification. *Pattern Recognit. Lett.* **2002**, *23*, 1419–1426. [[CrossRef](#)]
30. Yong, Z.; Kaufman, A.; Toga, A.W. Three-dimensional skeleton and centerline generation based on an approximate minimum distance field. *Vis. Comput.* **1998**, *14*, 303–314. [[CrossRef](#)]
31. Ma, W.C.; Wu, F.C.; Ouhyoung, M. Skeleton extraction of 3D objects with radial basis functions. In Proceedings of the International Conference on Shape Modeling International (SMI 2003), Seoul, South Korea, 12–15 May 2003; p. 207.
32. Lee, J.; Son, H.; Kim, C.; Kim, C. Skeleton-based 3D reconstruction of as-built pipelines from laser-scan data. *Autom. Constr.* **2013**, *35*, 199–207. [[CrossRef](#)]
33. Son, H.; Kim, C.; Kim, C. Fully Automated As-Built 3D Pipeline Extraction Method from Laser-Scanned Data Based on Curvature Computation. *J. Comput. Civ. Eng.* **2015**, *29*, B4014003. [[CrossRef](#)]
34. Oh, I.; Ko, K.H. Automated recognition of 3D pipelines from point clouds. *Vis. Comput.* **2021**, *37*, 1385–1400. [[CrossRef](#)]
35. Cheng, L.L.; Wei, Z.; Sun, M.C.; Xin, S.Q.; Sharf, A.R.E.; Li, Y.Y.; Chen, B.Q.; Tu, C.H. DeepPipes: Learning 3D pipelines reconstruction from point clouds. *Graph. Models* **2020**, *111*, 101079. [[CrossRef](#)]
36. Son, H.; Kim, C.; Kim, C. Automatic 3D Reconstruction of As-Built Pipeline Based on Curvature Computations from Laser-Scanned Data. In Proceedings of the Construction in a Global Network. 2014 Construction Research Congress, Atlanta, GA, USA, 19–21 May 2014; pp. 925–934.
37. Hu, Q.; Yang, B.; Xie, L.; Rosa, S.; Guo, Y.; Wang, Z.; Trigoni, N.; Markham, A. RandLA-Net: Efficient Semantic Segmentation of Large-Scale Point Clouds. In Proceedings of the 2020 IEEE/CVF Conference on Computer Vision and Pattern Recognition (CVPR), Seattle, WA, USA, 13–19 June 2020; pp. 11105–11114. [[CrossRef](#)]
38. Campello, R.J.G.B.; Moulavi, D.; Sander, J. Density-based clustering based on hierarchical density estimates. In Proceedings of the Advances in Knowledge Discovery and Data Mining. 17th Pacific-Asia Conference (PAKDD 2013), Gold Coast, Australia, 14–17 April 2013; pp. 160–172. [[CrossRef](#)]
39. Tagliasacchi, A.; Zhang, H.; Cohen-Or, D. Curve Skeleton Extraction from Incomplete Point Cloud. *Acm Trans. Graph.* **2009**, *28*, 1–9. [[CrossRef](#)]
40. Anil, E.B.; Tang, P.B.; Akinci, B.; Huber, D. Deviation analysis method for the assessment of the quality of the as-is Building Information Models generated from point cloud data. *Autom. Constr.* **2013**, *35*, 507–516. [[CrossRef](#)]
41. Huang, H.; Wu, S.H.; Cohen-Or, D.; Gong, M.L.; Zhang, H.; Li, G.Q.; Chen, B.Q. L1-Medial Skeleton of Point Cloud. *Acm Trans. Graph.* **2013**, *32*, 1–8. [[CrossRef](#)]
42. Junjie, C.; Tagliasacchi, A.; Olson, M.; Hao, Z.; Zhinxun, S. Point Cloud Skeletons via Laplacian Based Contraction. In Proceedings of the Shape Modeling International (SMI 2010), Aix-en-Provence, France, 21–23 June 2010; pp. 187–197. [[CrossRef](#)]

**Disclaimer/Publisher’s Note:** The statements, opinions and data contained in all publications are solely those of the individual author(s) and contributor(s) and not of MDPI and/or the editor(s). MDPI and/or the editor(s) disclaim responsibility for any injury to people or property resulting from any ideas, methods, instructions or products referred to in the content.